

OPTIMAL DOMAIN DECOMPOSITION STRATEGIES

Yonghyun Yoon*
Department of Aerospace Engineering
Korea Air Force Academy
Cheong-Ju, Korea

and

Bharat K. Soni**
NSF Engineering Research Center for
Computational Field Simulation
Mississippi State University
Mississippi State, Mississippi

ABSTRACT

The primary interest of the authors is in the area of grid generation, in particular, optimal domain decomposition about realistic configurations. A grid generation procedure with optimal blocking strategies has been developed to generate multi-block grids for a circular-to-rectangular transition duct. The focus of this study is the domain decomposition which optimizes solution algorithm/block compatibility based on geometrical complexities as well as the physical characteristics of flow field. The progress realized in this study is summarized in this paper.

INTRODUCTION

Most solution algorithms for irregular configurations presently solve a discrete form of the fluid equations of motion. The discretized equations must be solved on a discretized computational region, that is, on the grid nodes. A discretization process of grid generation is to establish a relationship between the physical and computational domain, thus allow the solution algorithm to be performed in the transformed domain.

In principle it is possible to make a correspondence between any physical region and a single computational region. However, for general complicated three-dimensional configurations the resulting grid is likely to exhibit excessive skewness and coarseness. Despite the power and sophistication of present grid generation capabilities, it remains difficult to generate a reasonable, single-block grid about geometrically complex flow field configuration.

* Assistant Professor of Korea Air Force Academy

**Professor of Aerospace Engineering, Mississippi State University

A better approach with complicated physical boundaries is to decompose the physical domains, each bounded by six curved sides and each of which transforms to a rectangular block in the computational domain(ref.1). This domain decomposition has the merits of flow solver efficiency, grid smoothness and orthogonality, and flexibility of gridding for complex geometries by choosing suitable block topologies.

There are many approaches and philosophies which can be included under the domain decomposition strategies. Structured grid analysis of flow around complex geometries in widespread use is blocked decomposition, in which the solution domain is divided into regions with common internal boundaries. The grid lines at adjoining blocks can be set up to match in a variety of ways, with various levels of slope continuity. There is no theory which governs the way in which a flow field should be partitioned. A limited number of papers in the literature(ref.2-5) address basic flow-field-decomposition criteria and guidelines. Eiseman has developed an automatic block decomposition algorithm(ref.6). This algorithm is based on the geometrical complexities. However, no comprehensive, systematic studies have been done to determine the effect on the computed solution of using different blocks for the same geometry. Currently, the major bottleneck is in the design and implementation of the blocking plane(ref.7)

To remedy this problem, the focus of this study is the domain decomposition which optimizes algorithm/block compatibility based on geometrical complexities as well as the physical characteristics of the flow field.

Generally, the use of analytical shapes is not enough to satisfy the unusual geometrical requirement. Hence, sculptured curve/surface definitions such as Non-Uniform Rational B-Splines(NURBS), and quick elliptic grid refinement algorithms are developed. The application of these algorithms to grid adaption and domain decomposition is demonstrated. Grid generation associated with the circular-to-rect angular transition duct has been accomplished by applying these techniques. After careful consideration of the various alternatives, the structured multi-block approach must be chosen as the most suitable, from the point of view both grid generation and flow analysis. INS3D(ref.8), a three-dimensional multi-block incompressible Navier-Stokes code is used for this study.

DOMAIN DECOMPOSITION PROCEDURE

The work focuses on effects for optimizing domain decomposition strategies associated with circular-to-rectangular transition duct. The transition duct is designed to connect a typical circular engine exhaust to a high aspect ratio rectangular nozzle. The application presented is of considerable engineering importance in internal fluid flow designs.

To take full advantage of the flexibility of multi-block structured techniques, one has to decide upon a suitable blocking topology to yield an optimal block arrangement for a given flow solver.

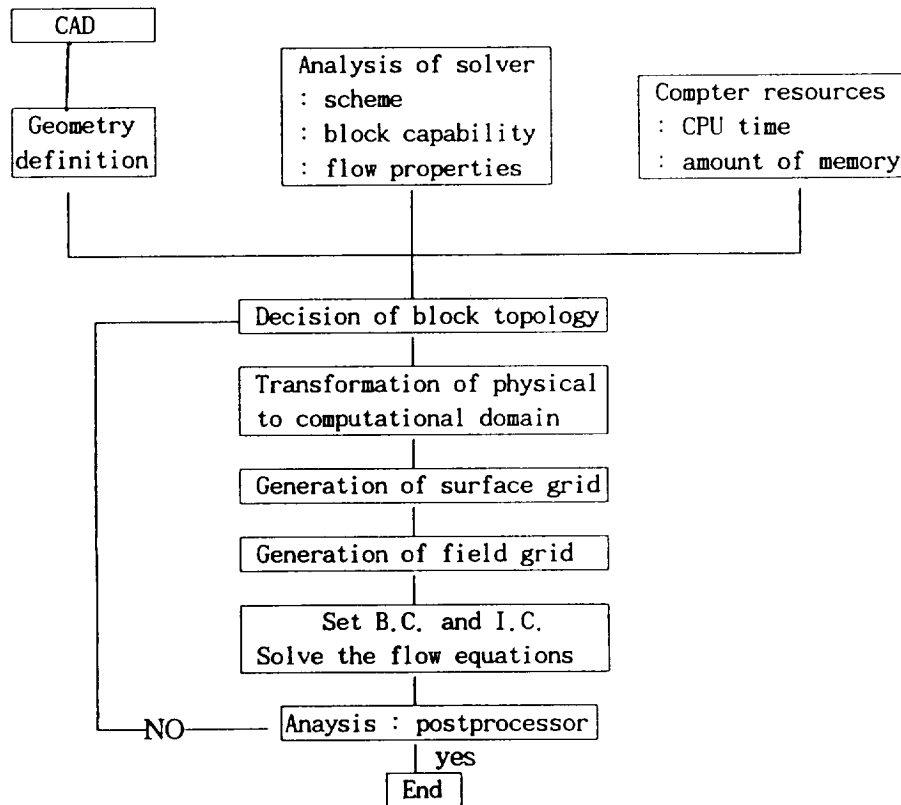


Figure 1. Basic procedure for domain decomposition

This step is an art, requiring knowledge-based techniques and trial-and-error. Typically, a domain decomposition strategy is performed and then surfaces and volume grids are created for each individual block. Figure 1 shows the basic procedure. The desired characteristics of multi-block grid are strongly dependent on the needs of the flow solver and computer.

GEOMETRY DEFINITION FOR TRANSITION DUCT

The circle-to-rectangular transition duct can be designed by the equation of a superellipse.

$$\left(\frac{y}{a}\right)^{\eta} + \left(\frac{z}{a}\right)^{\eta} = 1 \quad (1)$$

Where a and b are the semi-major and semi-minor axes, respectively, of the superellipse. The x axis is coincident with the streamwise direction and the y and z axes are parallel to the major and minor axes of the duct. The cross-sectional area at a given streamwise location is given by

$$A_{\infty} = \frac{\Gamma\left(\frac{1}{\eta}\right)^2}{\Gamma\left(\frac{1}{\eta}\right)} \left(\frac{2}{\eta}\right) (4ab) \quad (2)$$

Where η refers to the gamma function defined as

$$\Gamma(\eta) = \int_0^{\infty} (e^{-t} t^{\eta-1}) dt \quad (\eta > 0) \quad (3)$$

The design procedure for the transition duct is to specify the streamwise variation of the semi-major and semi-minor axes, and superellipse exponent(η) defined by fifth order polynomial functions. Special cases of the superellipse include a circle($a=b$, $\eta=\infty$), an ellipse($a \neq b$, $\eta=\infty$).

Steady, incompressible, turbulent, swirl-free flow through a circle-to-rectangular transition duct has been studied experimentally (ref.9). For comparison, the same geometry has been simulated. Figure 2 shows the lower half of the duct. The transition duct has an inlet diameter of 20.43cm, a length-to-diameter ratio of 1, and an exit plane

aspect ratio of three. The transition region length-to-diameter ratio is 1.5. The cross-sectional area remains the same at the exit as at the inlet, but varies through the transition section to a maximum value approximately 15% above the inlet value.

SURFACE REDISTRIBUTION AND REMAPPING

The principal requirement for generating a grid about a complex geometry is the ability to efficiently redistribute points on the surface while maintaining the integrity of the geometry. Because the regions where high gradients are expected in the flow solution require high density of grid points. The redistributed surface grid is accomplished by evaluating the NURBS surface at the respective parameter associated with the desired distribution space. The NURBS is used for the standard surface description. The convex hull, local support, and variation diminishing properties of B-spline functions contribute to the generation of the well-distributed smooth grid.

Let $\mathbf{r}=[x_1(\xi,\eta), x_2(\xi,\eta), x_3(\xi,\eta)]$ denote the parametric representation of the surface with coordinate (x_1, x_2, x_3) and parameter (ξ, η) . A control point form of the NURBS surface(in 3-D) is defined as a tensor product formula in 4-D(ref.10).

$$P(\xi, \eta) = \frac{\sum_{i=0}^{N_i} \sum_{j=0}^{N_j} B_i^M(\xi) B_j^K(\eta) H_{ij} Q_{ij}}{\sum_{i=0}^{N_i} \sum_{j=0}^{N_j} B_i^M(\xi) B_j^K(\eta) H_{ij}} \quad (4)$$

Where $B_i^M(\xi)$:the M^{th} degree B-spline basis functions in i direction.

$B_j^K(\eta)$:the K^{th} degree B-spline basis functions in j direction.

H_{ij} : weight (positive real values)

Q_{ij} : control points

The control points of the surface are determined using tensor product formula associated with both ξ and η parameters when a surface with a set of data point is given. It is called the inverse problem.

The parametric space associated with NURBS is transformed as the normalized arc length distribution mesh. The original surface which is expressed into non-NURBS form can be converted to NURBS representation. It is important to note that the redistributed surface grid

is obtained by evaluating the NURBS surface at the desired distribution point. However, the NURBS surface is smooth and has kept precisely the fidelity of the original surface. A redistributed surface resulting from the NURBS surface is demonstrated in Figure 3.

ELLIPTIC REFINEMENT

The grid should exhibit the desirable qualities of smoothness and orthogonality especially near the solid surface. Some results of algebraic grid methods such as transfinite interpolation functions can not meet the requirement of the grid qualities on certain geometries. Thus, elliptic grid methods are used to make up the shortcoming of the algebraic methods(ref.11).

Derivation of the control function based on grid metrics begins with analyzing the elliptic grid equation. Define the physical and computational space with $\mathcal{R}=(x_1, x_2, x_3)$ and $\mathcal{Q}=(\xi^1, \xi^2, \xi^3)$, respectively. The covariant and contravariant vectors then appear as follows:

$$a_i = \text{covariant base vectors } \mathcal{R}_{\xi^i} \quad (i=1, 2, 3)$$

$$a^i = \text{contravariant base vectors } \nabla \xi^i \quad (i=1, 2, 3)$$

$$g_{ij} = a_i \cdot a_j = g^{ij} \quad (i=1, 2, 3), (j=1, 2, 3)$$

$$g^{ij} = a^i \cdot a^j = g^{ij} \quad (i=1, 2, 3), (j=1, 2, 3)$$

$$g = \det|g_{ij}| = [a_1 \cdot (a_2 \times a_3)]^2$$

$$(g_{ij})_{\xi^k} \equiv \text{derivative of } g_{ij} \text{ with respect to } \xi^k$$

$$\equiv \mathcal{R}_{\xi^k} \mathcal{R}_{\xi^i} + \mathcal{R}_{\xi^i} \mathcal{R}_{\xi^k}, \quad (i=1, 2, 3), (j=1, 2, 3), (k=1, 2, 3)$$

The elliptic grid generation system used in this study(ref.12) is

$$\sum_{i=1}^3 \sum_{j=1}^3 g^{ij} \mathcal{R}_{\xi^i} \mathcal{R}_{\xi^j} + \sum_{k=1}^3 g^{kk} P_k \mathcal{R}_{\xi^k} = 0 \quad (5)$$

The determinations of the three control functions for the general three-dimensional case can be summarized as follows. The three components of the elliptic grid generation equation(5) provide a set of three equations,

$$\sum_{k=1}^3 g^{kk} (\mathcal{R}_{\xi^k})_l P_k = - \sum_{i=1}^3 \sum_{j=1}^3 g^{ij} (\mathcal{R}_{\xi^i})_l, \quad l=1, 2, 3 \quad (6)$$

that can be solved simultaneously at each point for the three control functions, P_k , $k=1, 2, 3$. The derivatives here are represented by central differences. The smoothness is established by replacing the control function at each point with the average of the four neighbors in the two curvilinear directions other than that of the function. Thus,

$$P_1(\xi^1, \xi^2, \xi^3) = \frac{1}{4} [P_1(\xi^1, \xi^2+1, \xi^3) + P_1(\xi^1, \xi^2-1, \xi^3) + P_1(\xi^1, \xi^2, \xi^3+1) + P_1(\xi^1, \xi^2, \xi^3-1)], \quad (7)$$

with analogous equations for P_2 and P_3 . No smoothing is done in the direction of the function because to do so would smooth the spacing distribution. The use of smoothed control functions evaluated from the algebraic grid produces a smooth grid that retains essentially the spacing of the algebraic grid(ref.13).

An application of these control functions results in a smooth-nearly orthogonal grid in fewer iterations of the elliptic solver. These control functions are applied in surface/volume grid refinement. It can be observed that the elliptic grid provides smoothness and near orthogonality in Figure 4.

BLOCK INTERFACES

There are three distinct configurations along the axial direction which are a constant diameter circular entrance section, the transition section, and a rectangular extension section. Because of the drastic changes in the flow direction, a multi-block grid topology has been adapted. This provides a smooth discretization of the entire volume inside the transition duct.

Each block has its own curvilinear coordinate system irrespective of that in the adjacent blocks. In order to keep complete continuity of grid lines across the interfaces between blocks, the linkage among the various blocks can be set by interpolation or fixing an actual boundary. The grid points on an interface of one block are coincident in physical space with those on another interface of the same or another block. This facilitates the interface of block treatment without an application of interpolation. This philosophy allows the flow solver to be run on the multi-block grid system.

APPLICATION

The two previously described methods, elliptic and algebraic, are merged appropriately to obtain various multi-block grids on the transition duct configuration. Moreover, by utilizing an appropriate blending of these methods allows a grid generation capability ranging from cases with only a few blocks to cases with hundreds of blocks for various shapes.

To demonstrate the capability of the present procedure, several types of multi-block grids are designed such that the grid cell aspect ratio and orthogonality are maintained with a reasonable range for all the duct cross section. Figure 5-8 present several examples. For comparative purposes, all types of domain decomposition are implemented in the same flow solver code using equivalent boundary conditions. Even the flow conditions for the computational analysis are chosen to correspond to the experiments reported in Ref.8. Inlet conditions are as follows:

Reynolds number = 390,000(based on U and D)

Bulk velocity(U) = 29.95 m/s

Core velocity(U_c/U) = 1.083

Friction velocity(U_{τ}/U) = 0.04063

RESULTS AND DISCUSSION

The results of the flow calculation are shown in Figures 9-12. Pressure contours of the axial flow component are plotted in Figure 9 (a)-(b) which are on the x-y plane and x-z plane, respectively. The velocity contours on both planes are demonstrated in Figure 10.(a)-(b). The transition segment produces saddle-shaped pressure distributions in the y-z plane as shown in Figure 11. Within the boundary layer the velocity is reduced as shown in Figure 12, but the cross-stream pressure gradient imposed by the flow outside the boundary layer is not reduced. This can result in significant flow turning in the boundary layer and is referred to as skew-induced secondary flow or cross flow. The rate of cross flow production increases as the amount of streamline curvature increases(ref.13). Figure 13 shows the comparison of sidewall normalized static pressure between the experimental data and the computed solutions in the upper quarter of the duct only. The results of computational simulation and the measured data of Ref.9., show a very good agreement.

CONCLUSIONS

Several blocking strategies have been considered in order to analyze the transition duct flow. Optimal domain decomposition is dependent on the method of flow solver and flow properties as well as geometry concerns. This domain decomposition gives us the following merits:

- A higher solution accuracy and faster convergence for the computational fluid dynamics solver.
- Savings in the CPU time and the amount of memory.
- Maximization of the grid quality and optimization of the grid distribution.

REFERENCES

1. Thompson, J. F., : A General Three-Dimensional Elliptic Grid Generation System on A Composite Block Structure, *Computer Methods in Applied Mechanics and Engineering*, p.377, 1987.
2. Allwright, S. E., : Techniques in Multi-Block Domain Decomposition and Surface Grid Generation, *Numerical Grid Generation in Computational Fluid Mechanics '88*, pp.559-568, Pineridge Press Limited, Mumbles, Swansea, U.K., 1988.
3. Piperni, P. : Multiblock Grid Generation with CAD-Based Domain Decomposition Techniques, *Numerical Grid Generation in Computational Fluid Dynamics and Related Fields*, pp.109-121, Pineridge Press Limited, Mumbles, Swansea, U.K., 1994
4. Rossow, C. C. and Ronzheimer, A., : Multi-Block Grid Generation around Wing-Body-Engine-Pylon Configurations, *Numerical Grid Generation in Computational Fluid Dynamics and Related Fields*, North-Holland, New York, 1991.
5. Vogel, A. A., : A Knowledge-Based Approach to Automated Flow-Field Zoning for Computational Fluid Dynamics, NASA TM101072, 1989.
6. Eiseman, P. R. etc, : Applications of Multi-Block Grid Generations with Automatic Zoning, *Numerical Grid Generation in Computational Fluid Dynamics and Related Fields*, Pineridge Press Limited, Mumbles, Swansea, pp.123-134. U.K., 1994

7. Danneffer, J. F., : A Block-Structuring Technique for General Geometries, AIAA Paper 91-0145, Jan. 1991.
8. Rogers, S. E., Kwak, D. C., and Chang, J. L. C., : INS3D- An Incompressible Navier-Stokes Code in Generalized Three-Dimensional Coordinates, NASA TM100012, 1987.
9. Davis, D. O., : Experimental Investigation of Turbulent Flow Through a Circle-To-Rectangular Transition Duct., NASA TM105210, 1992.
10. Yoon, Y. H., : Enhancements and Extensions of EAGLE Grid Generation System, Ph.D, Dissertation, Mississippi State University, 1991.
11. Thompson, J. F. Warsi, Z.U.A. and Mastin, C. W. : Numerical Grid Generation, Foundations and Applications, North-Holland , 1985.
12. Thompson, J. F. : Program EAGLE, Numerical Grid Generation System User's Manual, Vols. II and III, AFATL-TR-87-15, 1988.
13. Reichert, B. A., Hingst, W. R., and Okiish, : Circular-to-Rectangular Transition Duct Flow without and with Inlet Swirl, Journal of Propulsion and Power. Vol.10, No.1, Jan-Feb. 1994.

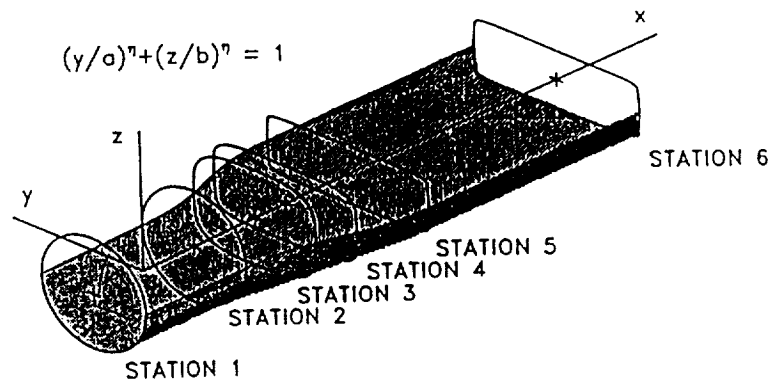


Figure 2. The lower half of the duct

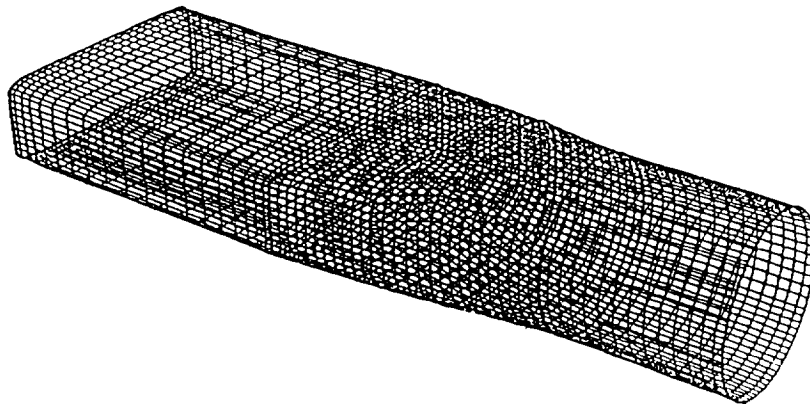


Figure 3. A NURBS surface

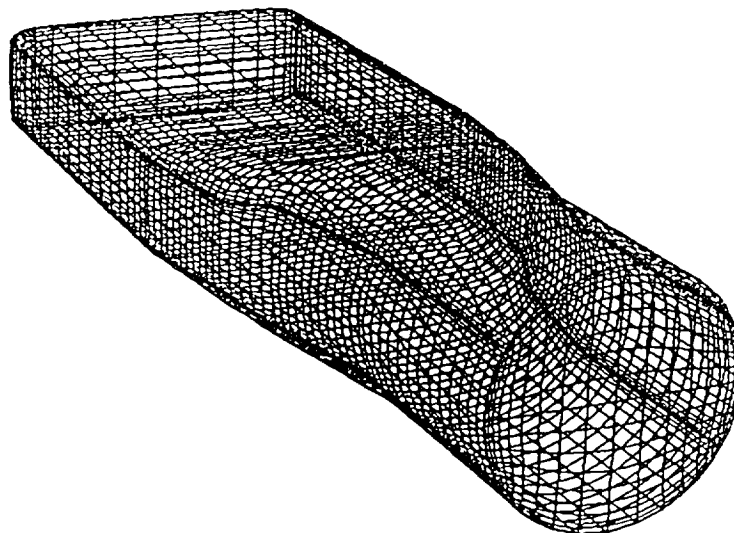


Figure 4. Elliptic grid refinement

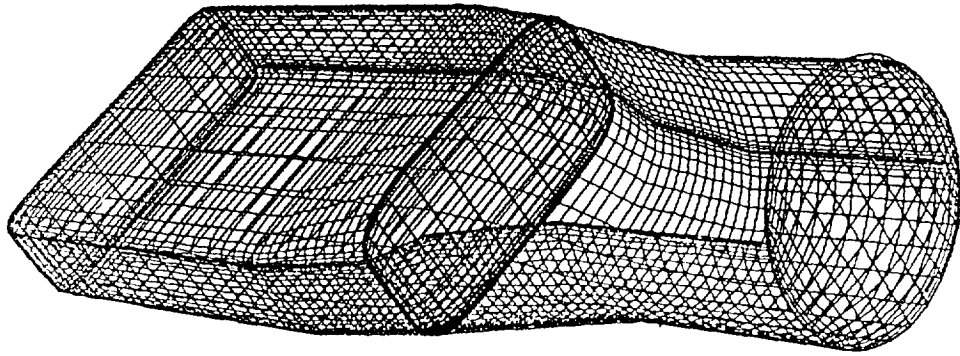


Figure 5. Two-block system along the flow direction

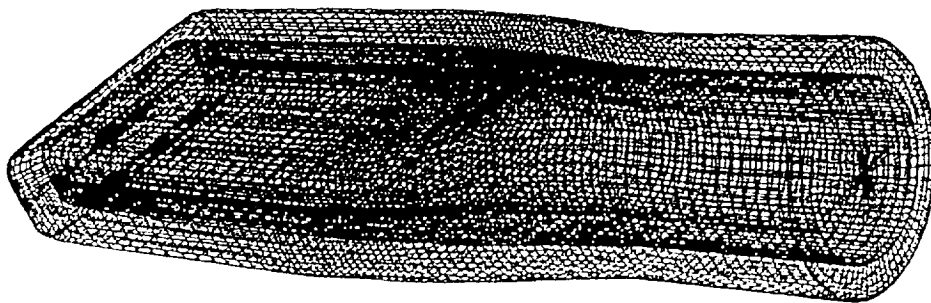


Figure 6. Two blocks, O-type grid system.

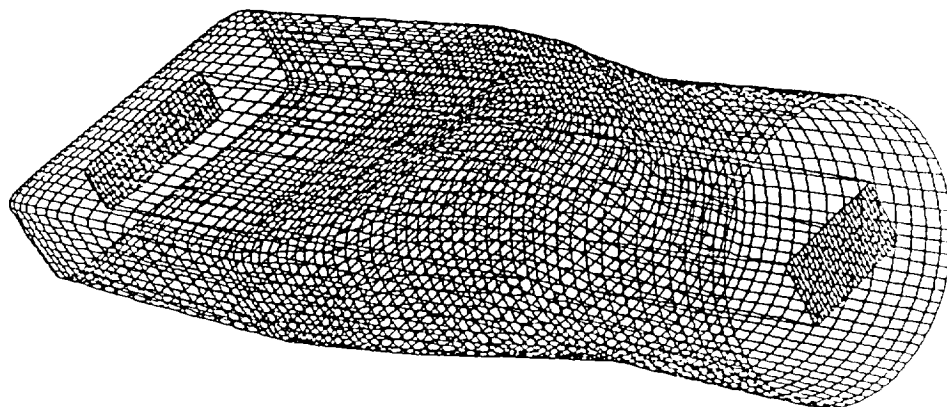


Figure 7. Two blocks, O-H type grid system.

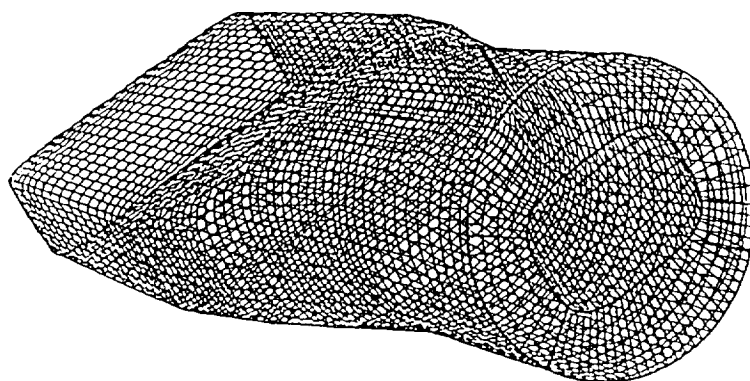


Figure 8. 5 blocks H-type grid system.

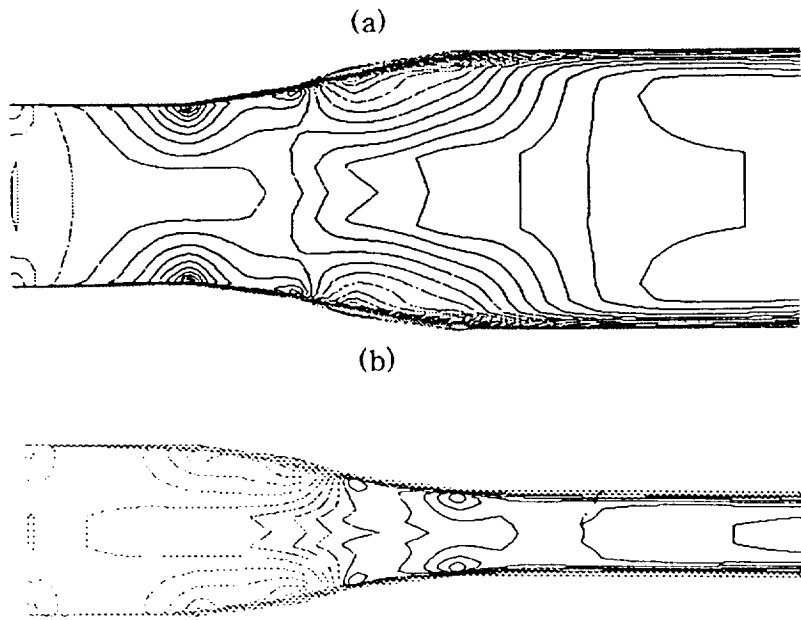


Figure 9. Pressure contours (a)x-y plane, (b)x-z plane.

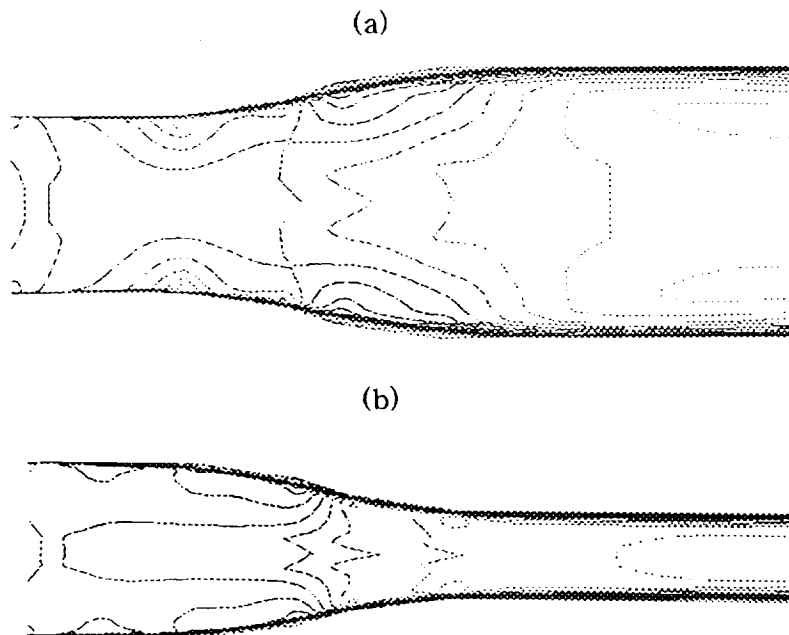


Figure 10. Velocity contours (a)x-y plane, (b)x-z plane.

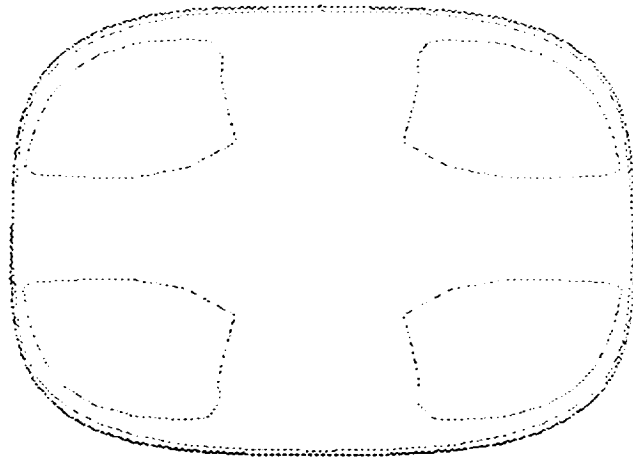


Figure 11. Vorticity contours.

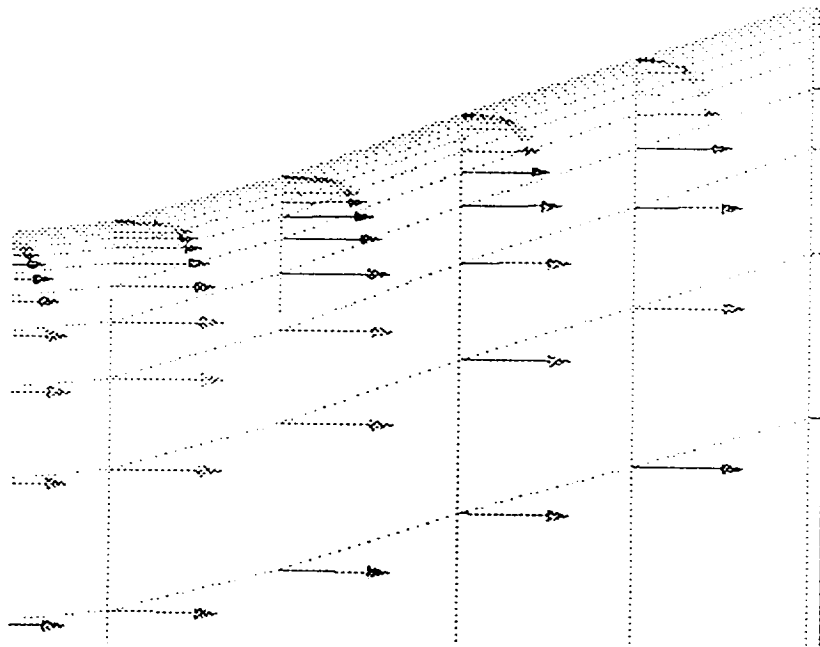


Figure 12. Boundary layer effects.

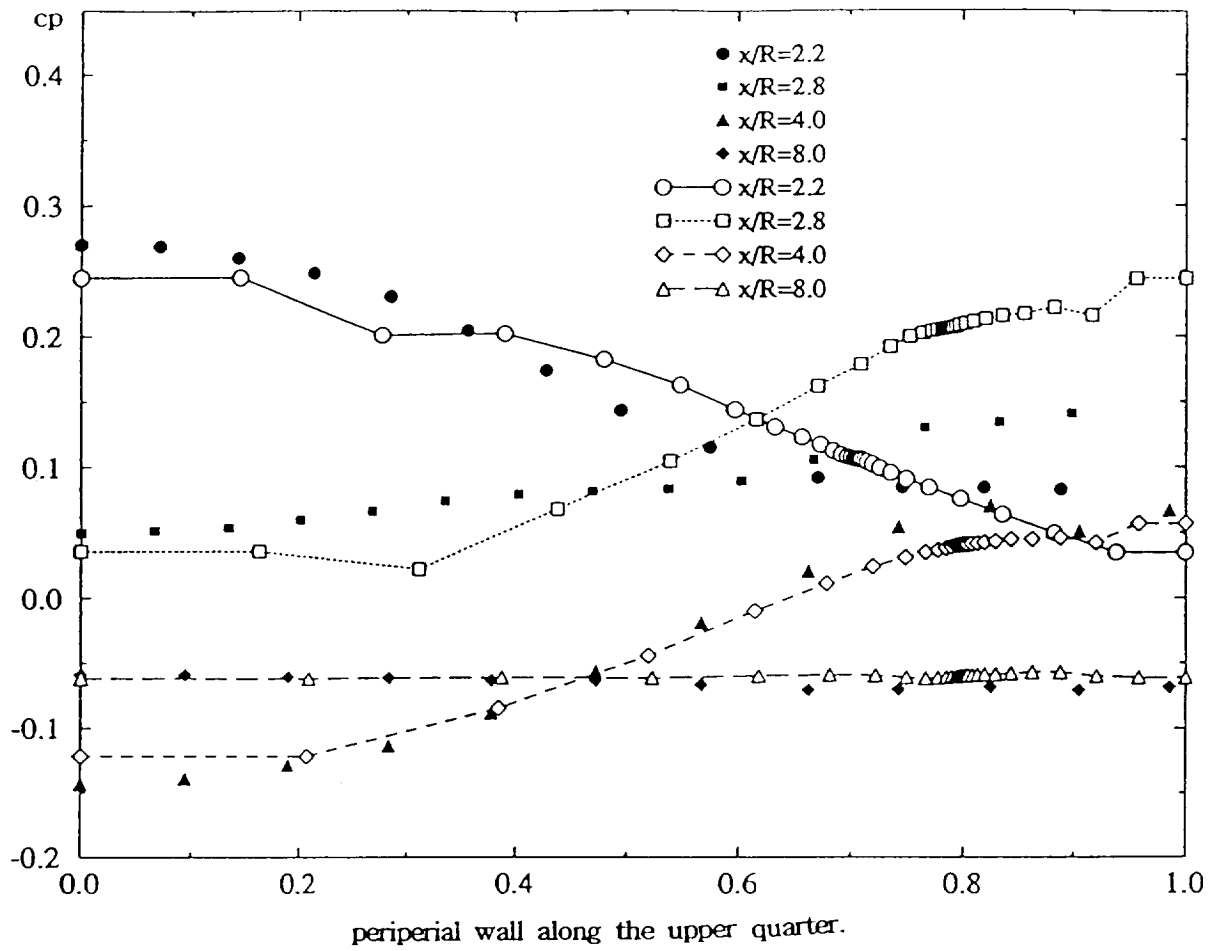


Figure 13. Comparison of periperial wall pressure coefficient distribution between computed and measured data. (symbol: experiment, simbol-line:calculation)



NEW METHODS/APPROACHES/
APPLICATIONS (1)

